A&A 554, A114 (2013)
DOI: 10.1051/0004-6361/201321394

Astronomy & Astrophysics

KOI-200 b and KOI-889 b: Two transiting exoplanets detected and characterized with *Kepler*, SOPHIE, and HARPS-N

G. Hébrard[1,2], J.-M. Almenara[3], A. Santerne[3,4], M. Deleuil[3], C. Damiani[3], A. S. Bonomo[3,5], F. Bouchy[3], G. Bruno[3], R. F. Díaz[3], G. Montagnier[1,2], and C. Moutou[3]

[1] Institut d'Astrophysique de Paris, UMR7095 CNRS, Université Pierre & Marie Curie, 98bis boulevard Arago, 75014 Paris, France
e-mail: hebrard@iap.fr
[2] Observatoire de Haute-Provence, CNRS/OAMP, 04870 Saint-Michel-l'Observatoire, France
[3] Aix Marseille Université, CNRS, LAM (Laboratoire d'Astrophysique de Marseille) UMR 7326, 13388 Marseille, France
[4] Centro de Astrofísica, Universidade do Porto, Rua das Estrelas, 4150-762 Porto, Portugal
[5] INAF – Osservatorio Astrofisico di Torino, via Osservatorio 20, 10025 Pino Torinese, Italy

Received 3 March 2013 / Accepted 22 April 2013

ABSTRACT

We present the detection and characterization of the two new transiting, close-in, giant extrasolar planets KOI-200 b and KOI-889 b. They were first identified by the *Kepler* team as promising candidates from photometry of the *Kepler* satellite; we then established their planetary nature thanks to the radial velocity follow-up jointly secured with the spectrographs SOPHIE and HARPS-N. Combined analyses of the whole datasets allow the two planetary systems to be characterized. The planet KOI-200 b has mass and radius of $0.68 \pm 0.09\ M_{\rm Jup}$ and $1.32 \pm 0.14\ R_{\rm Jup}$; it orbits in 7.34 days a F8V host star with mass and radius of $1.40^{+0.14}_{-0.11}\ M_\odot$ and $1.51 \pm 0.14\ R_\odot$. The planet KOI-889 b is a massive planet with mass and radius of $9.9 \pm 0.5\ M_{\rm Jup}$ and $1.03 \pm 0.06\ R_{\rm Jup}$; it orbits in 8.88 days an active G8V star with a rotation period of 19.2 ± 0.3 days, and mass and radius of $0.88 \pm 0.06\ M_\odot$ and $0.88 \pm 0.04\ R_\odot$. Both planets lie on eccentric orbits and are located just at the frontier between regimes where tides can explain circularization and where tidal effects are negligible. The two planets are among the first detected and characterized thanks to observations secured with HARPS-N, the new spectrograph recently mounted at the Telescopio Nazionale *Galileo*. These results illustrate the benefits that could be obtained from joint studies using two spectrographs as SOPHIE and HARPS-N.

Key words. planets and satellites: detection – techniques: photometric – techniques: radial velocities – techniques: spectroscopic – stars: individual: KOI-200 (Kepler-74) – stars: individual: KOI-889 (Kepler-75)

1. Introduction

Exoplanets transiting in front of their host stars allow numerous key studies to be performed, including accurate radius, mass, and density measurements, atmospheric studies in absorption through transits and in emission through occultations, dynamic analyses from possible timing variations, or obliquity measurements (see, e.g., Winn 2010 for a review). Today, nearly 300 transiting exoplanets have been discovered. They were mainly detected by ground-based photometric surveys which are mostly sensitive to close-in giant planets (see, e.g., Hébrard et al. 2013), and from their space-based counterparts CoRoT and *Kepler* which are sensitive to similar planets, as well as to planets on longer periods and/or smaller radii. The *Kepler* satellite, in particular, is monitoring stars with high-precision optical photometry with the goal of detecting signatures of exoplanetary transits. About 156 000 stars with magnitudes $9 < V < 16$ have been continuously observed by *Kepler* for more than three years now. Several candidate lists have been successively released by Borucki et al. (2011a,b) then Batalha et al. (2013), with a list now consisting of 2321 *Kepler* objects of interest (KOIs). An additional set of 461 new *Kepler* planet candidates has been recently announced by Burke et al. (2013). That dataset provides precious inputs for exoplanetology research, for statistical analyses as well as for individual studies on particular KOIs. However, in most cases photometry alone does not allow the planetary nature of the detected transits to be established. Indeed, several stellar configurations can mimic planetary transits (e.g., Almenara et al. 2009; Bouchy et al. 2009a), including undiluted eclipsing binaries with low-mass stellar companions or diluted eclipsing binaries, namely blends. Whereas such impostors represent the majority of transiting planet candidates detected by ground-based surveys or even by CoRoT, it has been argued from statistical studies that they should be particularly rare for *Kepler* candidates (e.g., Morton & Johnson 2011). Other studies have shown however that a significant part of the KOIs are actually not caused by planets but by scenarios implying stellar objects only (e.g., Bouchy et al. 2011; Colòn et al. 2012; Santerne et al. 2012). This is particularly true for close-in, giant exoplanet KOI candidates, whose false positive rate has been estimated at 34.8 ± 6.5% (Santerne et al. 2012) or 29.3 ± 3.1% (Fressin et al. 2013).

In numerous cases radial velocities (RV) allow blend scenarios and actual planetary transits to be distinguished. In addition to photometric data, radial velocities provide other parameters for the identified planetary systems; in particular, they allow the mass of the planets and the eccentricity of their orbits to be measured. In order to do these studies on *Kepler* candidates in 2010 we started a radial-velocity follow-up of KOIs with the SOPHIE spectrograph at the Observatoire de Haute-Provence (OHP, France). We mainly focused on the brightest stars (*Kepler* magnitude $K_{\rm p} < 14.7$) harboring candidates of

Table 1. IDs, coordinates, and magnitudes of the planet-host stars.

Object	KOI-200	KOI-889
Kepler ID	6046540	757450
USNO-A2 ID	1275-11623662	11200-11449160
2MASS ID	19322220+4121198	19243302+3634385
RA (J2000)	19:32:22.21	19:24:33.02
DEC (J2000)	41:21:19.87	36:34:38.57
Kepler magn. K_p	14.41	15.26
GSC-*V*	14.23	–
SDSS-*G*	14.876	15.998
SDSS-*R*	14.350	15.207
SDSS-*I*	14.212	14.949
2MASS-*J*	13.306 ± 0.024	13.665 ± 0.021
2MASS-*H*	13.008 ± 0.025	13.262 ± 0.025
2MASS-K_s	12.958 ± 0.033	13.118 ± 0.029
WISE-*W*1	12.857 ± 0.025	13.149 ± 0.025
WISE-*W*2	12.912 ± 0.029	13.286 ± 0.035
WISE-*W*3	12.307 ± 0.215	–

close-in, giant planets. In particular, this has already allowed us to identify and characterize several new transiting planets (Santerne et al. 2011a,b; Bonomo et al. 2012), as well as more massive companions and false positives (Ehrenreich et al. 2011; Bouchy et al. 2011; Santerne et al. 2012; Díaz et al. 2013).

The installation of the HARPS-N spectrograph at the Telescopio Nazionale *Galileo* (TNG, La Palma, Spain) gives us the opportunity to extend that on-going program. Indeed, HARPS-N is supposed to reach a better radial-velocity precision than SOPHIE, especially for faint *Kepler* targets thanks to the 3.58-m diameter of the TNG, to be compared with the 1.93-m diameter of the OHP telescope hosting SOPHIE. One of the main objectives of HARPS-N is the RV follow-up of the *Kepler* candidates. First, we used HARPS-N to follow KOIs for which our SOPHIE data suggested planet detection, but with a precision preventing firm conclusion and accurate characterization. Secondly, we also used HARPS-N to follow KOIs fainter than the limit $K_p = 14.7$ adopted with SOPHIE. We present here two new transiting planet detections, one in each of the two categories. This illustrates the benefits that could be obtained from joint studies using two spectrographs such as HARPS-N and SOPHIE for the follow-up of transiting planet candidates. We describe the photometric and spectroscopic observations of both targets in Sect. 2 and the analysis of the whole datasets and the results in Sect. 3. Tidal evolution of both planets is discussed in Sect. 4 and we conclude in Sect. 5.

2. Observations and data reduction

2.1. Photometric detection with Kepler

The IDs, coordinates, and magnitudes of the two targets are reported in Table 1. Both KOI-200 and KOI-889 has been observed by *Kepler* since the beginning of the mission in May 2009. They were identified by Borucki et al. (2011a,b) and Batalha et al. (2013) as hosting single periodic transits with periods of 7.34 and 8.88 days and depths characteristic of giant planets (Fig. 1). No transits with different periods were detected in any of the light curves, so there are no signs for multiple transiting systems. The *Kepler* photometry was acquired with a time sampling of 29.4 min (long-cadence data). The *Kepler* observations are divided in quarters; at the time of writing this paper, the 13 first quarters observed so-far by *Kepler* were publicly

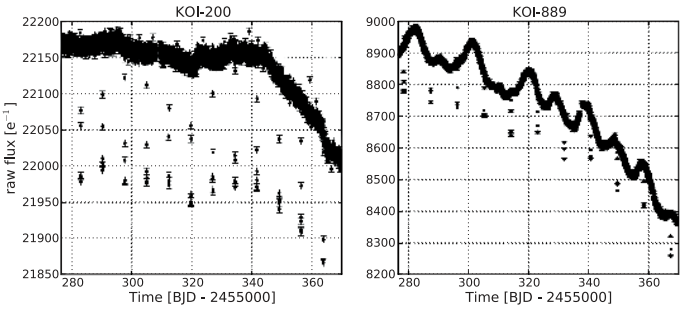

Fig. 1. Time samples of the *Kepler* light curves of KOI-200 and KOI-889 (Q5 data only). The signatures of periodic transits are easily detected, with periods of 7.34 and 8.88 days, respectively. In addition to the transit signal, the KOI-889 light curve shows a modulation with a period 19.2 days, which is probably due to spots appearing on the rotating surface of the star.

available from the MAST archive[1]. Some quarters were also observed in short cadence (every 1 min) for both targets. Since their transits in long-cadence data have been sampled sufficiently well, these short-cadence data were not used, which reduces computation time. We used the light-curve of quarters Q1 to Q13 reduced by the Photometric Analysis *Kepler* pipeline that accounts for barycentric, cosmic ray, background and so-called argabrightening corrections (Jenkins et al. 2010). Both light curves clearly present transits with depths of about 1% as reported by Borucki et al. (2011a,b) and Batalha et al. (2013), with a typical uncertainty per data point at the level of ~200 ppm for KOI-200 and ~500 ppm for KOI-889. While the light curve of KOI-200 does not show any sign of stellar variability, KOI-889 shows flux modulations at levels between ~2% and ~4% peak-to-peak, depending on the epochs. An example is shown in the right panel of Fig. 1. This is most likely due to spots appearing with variable extents and locations on the rotating surface of the star. Analyses through Lomb-Scargle periodograms and autocorrelation functions provide the same values for the periodicity of the modulations, which corresponds to the rotational period of the star: $P_{rot} = 19.2 \pm 0.3$ days. This is nearly twice the orbital period of the planet. A stellar rotation period similar to the orbital period is unlikely because of the shape of the light curve and the periodogram.

Before modeling the transits, we normalized fragments of the light curves by fitting an out-of-transit parabola, first without accounting for contamination. Since the *Kepler* spacecraft rotates four times a year, the crowding values are different between seasons. We thus produced four crowding-uncorrected detrended light curves for both targets, one per season. This will allow us to account for differential crowding values, noises, and out-of-transit fluxes in the transit modeling and in the final error budget (see Sect. 3.2). The corresponding phase-folded light curves are plotted in the upper panels of Fig. 2.

2.2. Radial velocities with SOPHIE and HARPS-N

Both SOPHIE (Perruchot et al. 2008; Bouchy et al. 2009b) and HARPS-N (Cosentino et al. 2012) are cross-dispersed, stabilized echelle spectrographs dedicated to high-precision radial velocity measurements. Each of them is fed by a set of two optical fibers mounted at the focus of their telescope (1.93-m OHP for SOPHIE and 3.58-m TNG for HARPS-N). Their spectral

[1] http://archive.stsci.edu/kepler/data_search/search.php

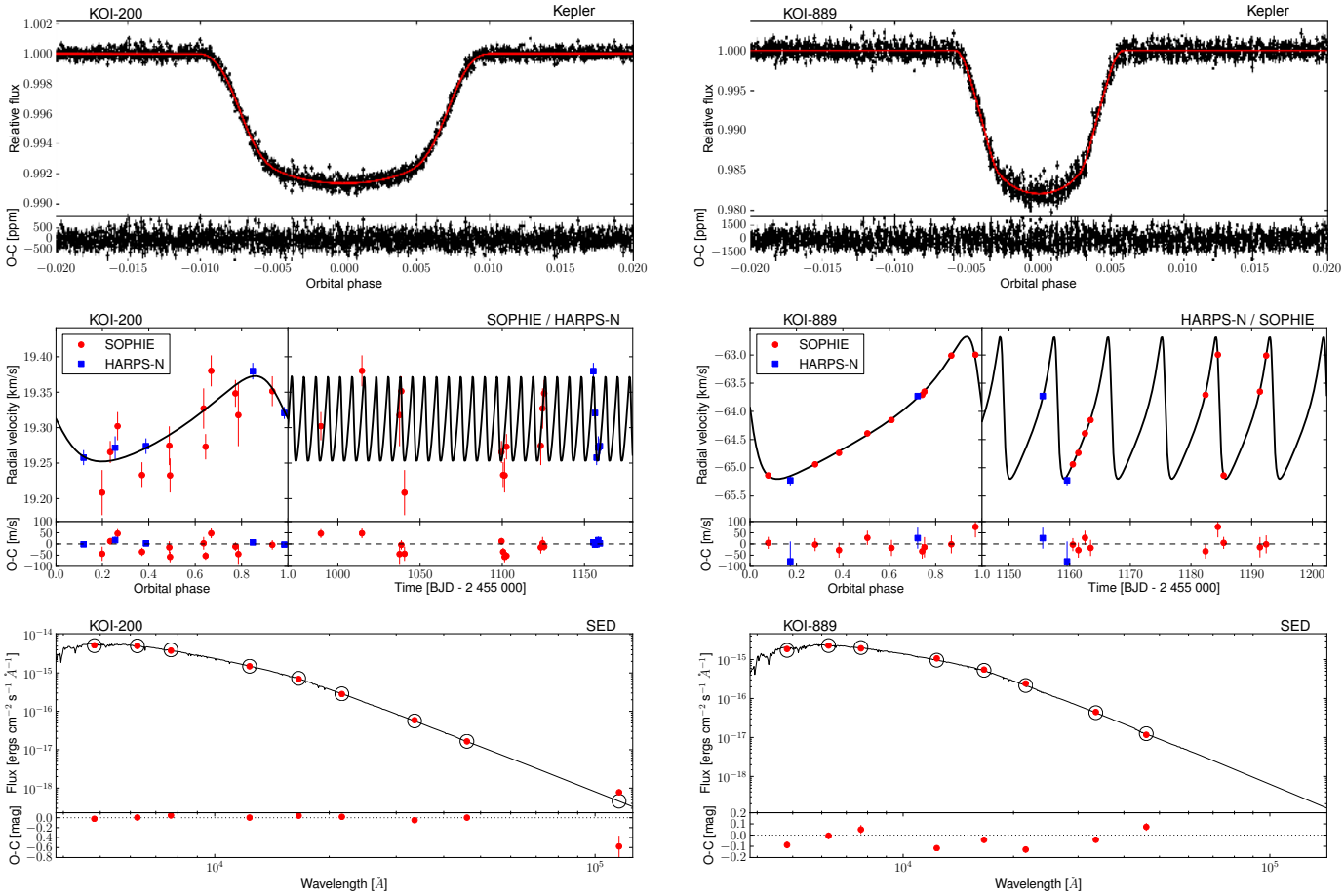

Fig. 2. Data and best-fit models for KOI-200 (*left*) and KOI-889 (*right*). The parameters of the fits are reported in Table 4. *Upper panels*: *Kepler* phase-folded light-curve (black dots with 1-σ error bars) over-plotted with the best model (red line), and residuals. *Middle panels*: SOPHIE (red circles) and HARPS-N (blue squares) radial velocities and 1-σ error bars phase-folded to the orbital period of the planet (*left*) or as function of time (*right*) over-plotted with the best model (black line), and residuals. *Lower panels*: fitted spectral energy distribution (black line) over-plotted with measured magnitudes (red circles, Table 1) and corresponding integrated flux in each of the photometric bands according to the fit (open circles).

ranges are similar (about 385 nm–693 nm) and their wavelength calibration is made using thorium-argon lamps. They are the only two spectrographs fed by octagonal-section fibers available now on the sky. This allows an improved stability and uniformity of the illumination for high-precision spectroscopy. SOPHIE was equipped by octagonal-section fibers in Spring 2011 (Bouchy et al. 2013) and HARPS-N since its start in Spring 2012. Both instruments are located in a thermally-controlled room, but while only the dispersive components are contained in a sealed constant-pressure tank in the case of SOPHIE, the whole HARPS-N instrument is encapsulated in a vacuum vessel which provides an even better radial-velocity stability. For the present studies SOPHIE was used in high-efficiency mode, yielding a resolution power $\lambda/\Delta\lambda = 40\,000$, whereas HARPS-N provides $\lambda/\Delta\lambda = 115\,000$. The slow read-out modes were used for the detectors of both instruments. The present HARPS-N observations were obtained just before the failure of the red side of the detector in late September 2012. For both stars and both instruments the two optical-fiber apertures (3″- and 1″-wide for SOPHIE and HARPS-N, respectively) were used. The first aperture was centered on the target and the second on the sky to simultaneously measure its background. It allowed us to confirm there was no moonlight pollution in any of our spectra significantly altering the radial velocity measurement. In the case of KOI-889 another star was coincidentally present in the second SOPHIE aperture. That second star does not affect the spectra extraction procedure for the first aperture, and we double-checked that there was no sky pollution using the observations of other targets secured on the nights we observed KOI-889.

The spectra were extracted from the detector images with the SOPHIE and HARPS-N pipelines. Based on similar structures, they include localization of the spectral orders on the 2D-images, optimal order extraction, cosmic-ray rejection, wavelength calibration, and corrections of flat-field. Then the spectra passed through weighted cross-correlation with G2-type numerical masks following the method described by Baranne et al. (1996) and Pepe et al. (2002). We adjusted the number of spectral orders used in the cross-correlations to reduce the dispersion of the measurements. Indeed, some spectral domains in the blue part of the spectra have particularly low signal-to-noise ratios (S/N), so using them degrades the precision of the radial-velocity measurement. In the end, we did not use the first 15 blue orders of the 70 available in the HARPS-N spectra for the cross-correlation, as well as the first 13 and 19 of the 39 SOPHIE orders for KOI-200 and KOI-889, respectively.

All the exposures provide a well-defined, single peak in the cross-correlation function (CCF). For KOI-200 their full widths at half maximum are 10.88 ± 0.12 km s^{-1} and their contrasts represent $23 \pm 4\%$ of the continuum for SOPHIE, the corresponding values for HARPS-N being 8.38 ± 0.06 km s^{-1} and $42.3 \pm 0.7\%$.

Table 2. SOPHIE and HARPS-N measurements for the planet-host stars KOI-200 and KOI-889.

BJD_{UTC} –2 450 000	RV (km s^{-1})	$\pm 1\sigma$ (km s^{-1})	Bisect.* (km s^{-1})	Exp. (s)	$S/N^{\dagger}$	Instr.‡
KOI-200:						
5989.6552	19.302	0.020	–0.106	2700	17.7	SOP
6014.6390	19.380	0.022	–0.034	2490	17.0	SOP
6037.5189	19.318	0.044	–0.206	3600	12.4	SOP
6038.5923	19.351	0.021	–0.048	3600	17.7	SOP
6040.5504	19.208	0.032	–0.031	3600	14.8	SOP
6099.5331	19.266	0.016	–0.020	3600	19.3	SOP
6100.5370	19.233	0.018	–0.054	3600	19.6	SOP
6101.4251	19.233	0.024	–0.016	3600	16.1	SOP
6102.5506	19.273	0.018	–0.063	3600	19.7	SOP
6123.4243	19.274	0.027	0.028	3600	13.5	SOP
6124.5103	19.327	0.028	–0.008	3600	15.4	SOP
6125.5146	19.348	0.019	–0.020	3600	16.9	SOP
6155.4268	19.430	0.012	0.051	2700	10.0	HAR
6156.4254	19.371	0.008	0.002	2700	15.2	HAR
6157.4150	19.308	0.011	0.029	2700	13.7	HAR
6158.4134	19.322	0.016	0.033	2700	8.6	HAR
6159.3891	19.324	0.011	0.019	2700	12.0	HAR
KOI-889:						
6155.5647	–63.682	0.047	0.052	1400	2.3	HAR
6159.5726	–65.177	0.089	–0.258	700	1.1	HAR
6160.5219	–64.940	0.029	–0.155	3600	12.2	SOP
6161.4375	–64.736	0.034	–0.033	3600	11.1	SOP
6162.5235	–64.390	0.032	–0.202	3600	10.1	SOP
6163.4458	–64.154	0.036	0.099	2716	9.4	SOP
6182.3935	–63.709	0.033	–0.075	3600	13.4	SOP
6184.4300	–62.995	0.047	–0.099	3600	7.1	SOP
6185.3837	–65.137	0.027	–0.012	3600	12.3	SOP
6191.3641	–63.649	0.045	–0.088	3600	11.8	SOP
6192.3927	–63.011	0.040	0.107	3600	12.2	SOP

Notes. (*) Bisector spans; associated error bars are twice those of RVs. (†) Signal-to-noise ratio per pixel at 550 nm. (‡) Instrument used: SOP for SOPHIE, HAR for HARPS-N.

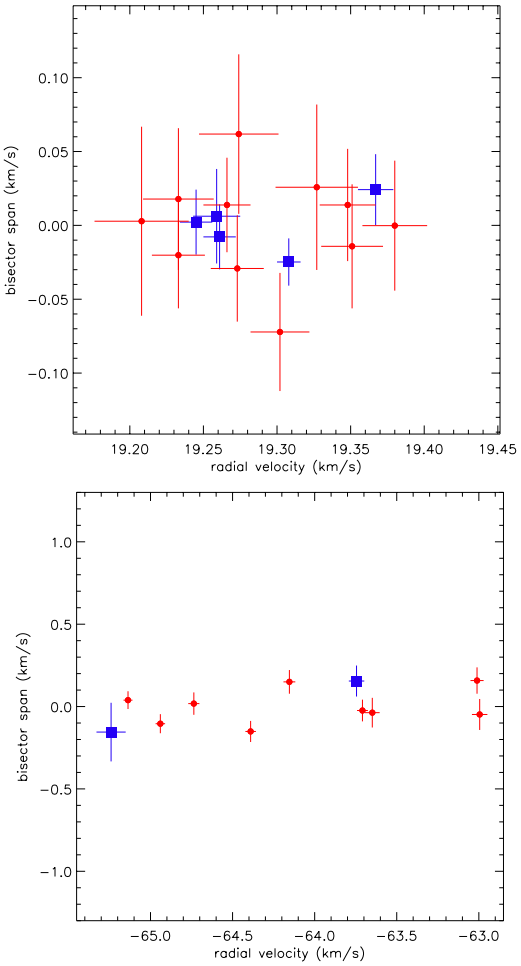

Fig. 3. Bisector span as a function of the radial velocities with 1-σ error bars for KOI-200 (*top*) and KOI-889 (*bottom*). SOPHIE data are red circles, and HARPS-N blue squares. The ranges have the same extents in the x- and y-axes on each figure.

In the case of KOI-889 the values are 10.17 ± 0.10 km s^{-1} and 21 ± 4% for SOPHIE, and 7.49 ± 0.14 km s^{-1} and 54.7 ± 1.2% for HARPS-N. The differences are mainly due to spectral resolutions of both instruments. The radial velocities were obtained from Gaussian fits of the CCFs, together with their associated error bars and bisector spans. They were also corrected from the interpolated drift of the spectrographs. The bisector span error bars were estimated to be two times those of the corresponding radial velocities. The measurements are reported in Table 2 and are plotted in Fig. 2 (middle panel) and Fig. 3.

In the case of KOI-200, we first obtained five SOPHIE exposures of ~1 h each in March-April 2012 that showed marginal radial velocity variations, possibly in agreement with the *Kepler* ephemeris. The hint of detection was reinforced with seven extra SOPHIE measurements secured in June–July 2012. However, the detection was at the limit of the SOPHIE capabilities with a semi-amplitude of the order of 50 m s^{-1}, whereas the SOPHIE measurements of KOI-200 typically have a ±25-m s^{-1} precision. So we re-observed KOI-200 with HARPS-N five nights in a row in August 2012, obtaining five 45-min exposures with better precision, between ±8 and ±16 m s^{-1}. The HARPS-N data sampled reasonably well the orbital phases of the 7.34-day period. They confirmed the planet detection and allowed a small eccentricity to be detected (Fig. 2, left, middle panel).

The target KOI-889 was fainter than our adopted magnitude limit on SOPHIE so first we secured two observations with HARPS-N in August 2012, near the quadratures according to the *Kepler* ephemeris. Because of technical issues and poor weather conditions, these exposures were short (23 and 12 min only) and provided poor signal-to-noise ratios, which limited the radial velocity precisions to ±47 m s^{-1} and ±89 m s^{-1}, respectively. However, the signal-to-noise was high enough to detect the 1.5-km s^{-1} variation between the two epochs. Such a large variation does not necessarily require HARPS-N, but is enough to be detected with SOPHIE despite the faintness of the target. So starting the following night we switched that target to SOPHIE and finally secured nine observations of KOI-889 in August-September 2012 at OHP, sampling the different orbital phases of the 8.88-day period. Thanks to better weather conditions and longer exposure times (~1 h per exposure), SOPHIE allowed an improved radial-velocity precision to be reached on that target (typically ±35 m s^{-1}) compared to HARPS-N.

For both targets, the joint SOPHIE and HARPS-N datasets show radial velocity variations in agreement with the *Kepler* ephemeris (Fig. 2, middle panel). They imply semi-amplitudes in two different regimes, $K \simeq 60$ m s^{-1} and $K \simeq 1300$ m s^{-1} for KOI-200 and KOI-889, respectively, corresponding to ~0.7 M_{Jup} and ~10 M_{Jup} for both companions: they lie in the planet-mass range. Radial velocities obtained using different stellar masks

(F0, G2, or K5) produce variations with similar amplitudes, so there is no evidence that the variations could be explained by blend scenarios caused by stars of different spectral types. Similarly, the cross-correlation function bisector spans show neither variations nor trends as a function of radial velocity (Fig. 3). A weak correlation could be seen in the case of KOI-889, but it mainly stands on the two low-S/N HARPS-N measurements. It disappears when only the nine higher-S/N SOPHIE measurements are considered. This reinforces the conclusion that the radial-velocity variations are not caused by spectral-line profile changes attributable to blends or stellar activity. We thus conclude that both targets harbor transiting giant planets, which we hereafter designate as KOI-200 b and KOI-889 b.

3. System characterization

3.1. Parameters of the host stars

The spectral analysis of both host stars was performed with the co-added individual spectra obtained with SOPHIE once reduced and set on the rest frame. In the case of KOI-200, the second aperture which is located on the sky was subtracted from each spectrum in order to correct from the residual background sky light. For KOI-889 this was not possible because of the other star coincidentally located in the second aperture, which implied a higher uncertainty here. The total signal-to-noise ratios of the co-added spectra are 75 and 64 per resolution element at 550 nm in the continuum, for KOI-200 and KOI-889, respectively.

We performed the spectral analysis using the iterative spectral synthesis package VWA. As described in detail by Bruntt et al. (2010) and references therein, the atmospheric parameters $T_{\rm eff}$, $\log g_*$, and [Fe/H] were derived from a set of 49 Fe I and nine Fe II carefully selected weak lines. Ionization and excitation equilibrium were imposed, as well as a zero slope between the abundances given by individual lines and their equivalent width. The SME package (version 2.1: Valenti & Piskunov 1996; Valenti & Fischer 2005) was also applied as a check to both stars and provided similar results to those obtained with VWA, but with slightly larger error bars. As an additional verification, we also derived the surface gravity from the Ca I pressure-sensitive line at 612.2 nm. The projected rotational velocity $v \sin i_*$ and the macroturbulence were determined independently from a set of isolated spectral lines in the case of KOI-200. The $v \sin i_*$ measurement agrees with that obtained from the width of the cross-correlation function (Sect. 2.2) following the method presented by Boisse et al. (2010). Because of the poor signal-to-noise ratio of the spectra, the $v \sin i_*$ of KOI-889 was only measured from the cross-correlation function.

The fundamental parameters of the two host stars (mass, radius, and age) were estimated from the comparison of the location of the star in the H-R diagram with StarEvol evolution tracks (Lagarde et al. 2012; Palacios, priv. comm.). We used the atmospheric parameters $T_{\rm eff}$ and [Fe/H] with their associated uncertainties and the distribution of stellar density derived from the transit model (see Sect. 3.2.1 below) in the χ^2 minimization as described by Santerne et al. (2011a) to derive the stellar masses, radii, and gravities.

The evolutionary tracks provide an age estimate of $2.9^{+1.5}_{-0.8}$ Gyr for KOI-200. We found two distinct sets of solutions for KOI-889: the first corresponds to a young star of 200 Myr and the second to a more evolved main-sequence star with an age of 10.2 ± 2.1 Gyr. The spectra of the star do not display any sign of chromospheric activity in the Ca II lines and the rotation period (Sect. 2.1) provides gyrochronological ages of 1.7 ± 0.4 Gyr and 3.1 ± 0.7 Gyr using the relations of Barnes (2007) and Lanza (2010), respectively. We thus favor the oldest solutions and finally adopt 6 ± 3 Gyr for the age of KOI-889.

The parameters of both stars derived from these procedures are given in Table 4. KOI-200 is a F8V star and KOI-889 a G8V star. Both are slowly rotating. Our derived parameters are in good agreement with those estimated from photometry in the *Kepler* Input Catalog (KIC, Brown et al. 2011) although our $T_{\rm eff}$, masses, and radii are slightly larger.

3.2. Parameters of the planetary systems

3.2.1. Method

The four normalized *Kepler* light curves constructed from quarters Q1 to Q13 (Sect. 2.1) were fitted together with SOPHIE and HARPS-N radial velocities (Sect. 2.2) using the PASTIS code (Díaz et al., in prep.). This code was used in previous analyses (e.g., Santerne et al. 2011b; Díaz et al. 2013; Kostov et al. 2013). The transit light curves were modeled using the EBOP code (Etzel 1981) extracted from the JKTEBOP package (Southworth et al. 2004). As recommended by Kipping (2010), we used an oversampling factor of five when comparing the model with the light curves to account for the long integration time of the *Kepler* light curve (Kipping & Bakos 2011). Radial velocity curves were simultaneously fitted with eccentric Keplerian orbit. No significant radial velocity drifts were detected so we assume only two bodies in each Keplerian fit. The radial velocity measurements are too sparse and the time spans are too short to allow useful constraints to be put on the presence of additional bodies in the systems. For each *Kepler* light curve we included the out-of-transit flux and the contamination factor as free parameters. Contamination factors reported in the KIC (Brown et al. 2011) have been shown to be incorrect in some cases (see, e.g., KOI-205; Díaz et al. 2013) so we chose to fit them instead of adopting the KIC values. We also account for additional sources of Gaussian noise in the light curves and radial velocities by fitting a jitter value to each data set. This is especially appropriate for the *Kepler* data since the star is located on different CCDs each season. The system and data are finally described by the 26 free parameters listed in Table 3. These parameters were fitted using a Metropolis-Hasting Markov Chain Monte Carlo (MCMC) algorithm (e.g., Tegmark et al. 2004; Ford 2006) with an adaptive step size (Ford 2006). To better sample the posterior distribution in case of non-linear correlations between parameters, we applied an adaptive principal component analysis to the chains and jumped the parameters in an uncorrelated space (Díaz et al., in prep.). Two additional parameters were not free; they were fixed in the analysis because they are negligible here in cases of exoplanets, whereas they could have significant effects for stellar binaries. The first is the gravity darkening coefficient fixed to $\beta_1 = 1$ (with $\beta_1 = 4 \times \beta$; see Espinosa Lara & Rieutord 2012). The second is the mass ratio which is fixed to 0; it constrains the ellipsoid modulations of the light curves which are not detected here.

Table 3 also lists the priors used for this analysis. Incorrect tabulated limb-darkening coefficients could alter the results (see, e.g., Csizmadia et al. 2013). In order to avoid underestimation of uncertainties, we chose to leave the limb-darkening coefficients free to vary instead of adopting tabulated values. Priors on the contamination factors were chosen according to the values provided by the KIC assuming 0.5% of Gaussian uncertainty. Priors on the orbital period and the epoch of first transit were centered

Table 3. List of free parameters and their priors used to model the data.

Parameter	Prior (values)[†]	
	KOI-200	KOI-889
Kepler photometry:		
season 0 out-of-transit flux	$\mathcal{N}(1, 1\times10^{-4})$	
season 1 out-of-transit flux	$\mathcal{N}(1, 1\times10^{-4})$	
season 2 out-of-transit flux	$\mathcal{N}(1, 1\times10^{-4})$	
season 3 out-of-transit flux	$\mathcal{N}(1, 1\times10^{-4})$	
season 0 contamination [%]	$\mathcal{N}(4.5, 0.5)$	$\mathcal{N}(10.4, 0.5)$
season 1 contamination [%]	$\mathcal{N}(3.5, 0.5)$	$\mathcal{N}(13.8, 0.5)$
season 2 contamination [%]	$\mathcal{N}(7.2, 0.5)$	$\mathcal{N}(16.0, 0.5)$
season 3 contamination [%]	$\mathcal{N}(4.7, 0.5)$	$\mathcal{N}(8.2, 0.5)$
season 0 jitter	$\mathcal{J}(1\times10^{-6}, 1\times10^{-2})$	
season 1 jitter	$\mathcal{J}(1\times10^{-6}, 1\times10^{-2})$	
season 2 jitter	$\mathcal{J}(1\times10^{-6}, 1\times10^{-2})$	
season 3 jitter	$\mathcal{J}(1\times10^{-6}, 1\times10^{-2})$	
Radial velocities:		
SOPHIE jitter [km s^{-1}]	$\mathcal{J}(1\times10^{-5}, 1)$	
HARPS-N jitter [km s^{-1}]	$\mathcal{J}(1\times10^{-5}, 1)$	
Systemic RV [km s^{-1}]	$\mathcal{U}(-100, 100)$	
Instruments offset [km s^{-1}]	$\mathcal{N}(0, 2)$	
Orbit and transit light curve:		
Orbital period [d]	$\mathcal{N}(7.341, 1\times10^{-4})$	$\mathcal{N}(8.885, 1\times10^{-4})$
Tr. epoch [BJD – 2 454 900]	$\mathcal{N}(67.34, 1\times10^{-3})$	$\mathcal{N}(102.99, 1\times10^{-3})$
System scale $a/R_\star$	$\mathcal{J}(6, 25)$	$\mathcal{J}(5, 70)$
Radius ratio $R_p/R_\star$	$\mathcal{J}(0.01, 0.2)$	
Orbital inclination [°]	$\mathcal{U}(70, 90)$	
Orbital eccentricity	$\mathcal{N}(0.29, 0.09)$	$\mathcal{U}(0, 1)$
Argument of periastron [°]	$\mathcal{U}(0, 360)$	
Linear limb darkening	$\mathcal{U}(-1.5, 1.5)$	
Quadratic limb darkening	$\mathcal{U}(-1.5, 1.5)$	
RV semi-amplitude [km s^{-1}]	$\mathcal{J}(1\times10^{-3}, 1)$	$\mathcal{J}(1\times10^{-2}, 10)$

Notes. [(†)] $\mathcal{N}(\mu, \sigma^2)$: normal distribution centered on μ with a width of σ; $\mathcal{J}(a, b)$: Jeffreys distribution between a and b; $\mathcal{U}(a, b)$: Uniform distribution between a and b. Prior values are discussed in Sect. 3.2.1.

on the value found by Batalha et al. (2013), with a width about 100 times larger than the reported errors to avoid biased solutions. In general, the shapes and widths of priors were chosen to be large enough to limit the bias on the posterior. For the eccentricity of KOI-200 b which is not well constrained in the SOPHIE data, we used as prior the posterior distribution of an independent MCMC analysis of the radial velocity alone in order to reach the convergence of the final MCMC more quickly. The two systems KOI-200 and KOI-889 were analyzed with 55 and 40 chains leading to a total of 7×10^7 and 4×10^7 steps, respectively. Each chain was started at random points drawn from the joint prior. In both cases, all chains converged to the same solution. We used a modified version of the Geweke (1992) diagnostic to determine and remove the burn-in phase of each chain. We then computed the correlation length of the converged sub-chains before thinning them. We finally merged the thinned chains, which left us with a total of about 1000 independent samples of the posterior distribution for both targets.

The distances of both stars were determined through another MCMC algorithm by comparing the magnitudes reported in Table 1 with an interpolated grid of synthetic spectra from the PHOENIX/BT-Settl library (Allard et al. 2012). We used the $T_{\rm eff}$, [Fe/H], and $\log g_*$ of the host star from the spectral analysis (see Sect. 3.1) with their respective errors as prior of the MCMC and left the distance and interstellar reddening as free parameters to fit the spectral energy distribution. This consisted in adjusting the stellar parameters within the prior to find the best synthetic spectrum that matches the observed magnitude after rescaling it from the distance luminosity of the star and correcting from the interstellar extinction.

3.2.2. Results

The 68.3% confidence intervals (corresponding to 1-σ intervals assuming Gaussian distributions) are listed in Table 4. The maximum posterior models are displayed in Fig. 2.

Our procedure and the quality of the *Kepler* data allow the contamination factors to be directly measured. They show slight variations between the four *Kepler* seasons, as expected because of the four different orientations of the satellite. Our derived values are similar to the ones reported in the KIC, but here we can determine their uncertainties. The derived jitter is around 100 ppm for KOI-200, which is compatible with the typical value derived by Gilliland et al. (2011) for the *Kepler* data (Díaz et al. 2013). In the case of KOI-889 we found ~300 ppm; the excess of jitter could be explained by the activity of the star. The jitters show some variations between seasons, probably linked to the different characteristics of the four different parts of the detector that are used each season. The out-of-transit fluxes fitted for each season were found near unity with typical uncertainties of ±8 ppm and ±25 ppm for KOI-200 and KOI-889, respectively. None of the light curves show the signature of planetary occultation at the secondary eclipse phase, as expected for relatively long-period planets such as these. Occultations depths are expected here to be at most of the order of a few tens of ppm. In addition, in the case of KOI-200 b, the secondary eclipse is likely to be un-observable from the Earth as the secondary impact parameter is $b_{\rm sec} = 1.11 \pm 0.23$. This is the case for a significant part of eccentric planets, even on close-in orbits (Santerne et al. 2013). In the case of the radial velocities, only the SOPHIE data for KOI-200 need a significant jitter of 28 ± 13 m s^{-1} to be added. For the other cases the dispersion of the residuals around the fit agrees with the expected error bars on the radial velocities.

From the results of the spectral analysis, we expect the limb-darkening coefficients from Claret et al. (2012) of $u_a = 0.34 \pm 0.02$ and $u_b = 0.30 \pm 0.10$ for KOI-200, and $u_a = 0.47 \pm 0.03$ and $u_b = 0.22 \pm 0.02$ for KOI-889. Our fitted limb-darkening coefficients are compatible with the expected values within 1-σ. Fixing the coefficients to the values from Claret et al. (2012) does not significantly change our results. Similarly, the $\log g_*$ values derived from the stellar spectra agree with those derived from the stellar density. And finally, the fit of the spectral energy distribution provides the distance and the interstellar extinction $E(B-V)$ of each target, as well as the stellar parameters $\log g_*$, $T_{\rm eff}$, and [Fe/H], which were found to agree with the values derived from the stellar analysis itself. Thus, the different analyses are coherent with respect to the different constraints they use.

Orbiting an F8 dwarf star in 7.340718 ± 0.000001 days, KOI-200 b is a giant planet with a mass of $0.68 \pm 0.09\ M_{\rm Jup}$ and a radius of $1.32 \pm 0.14\ R_{\rm Jup}$. Its density $\rho_{\rm p} = 0.37 \pm 0.13$ g/cm^3 is particularly low. Whereas the SOPHIE data alone do not allow a significant eccentricity to be detected, the five HARPS-N measurements exclude circularity for the orbit, with a residuals dispersion reduced from ±14 m s^{-1} to ±6 m s^{-1} between circular and eccentric orbits. The light curve also provides constraints on the eccentricity through the duration of the transit. In addition, in the case of a circular orbit the derived limb darkening coefficients agreed less well with the ones expected from spectral analysis according to Claret et al. (2012). With all the constraints

Table 4. Planetary and stellar parameters for the systems KOI-200 and KOI-889.

	KOI-200	KOI-889
Ephemeris and orbital parameters:		
Planet orbital period P [days]	7.340718 ± 0.000001	8.884924 ± 0.000002
Transit epoch T_0 [BJD – 2 454 900]	67.3453 ± 0.0003	102.9910 ± 0.0002
Periastron epoch T_p [BJD – 2 454 900]	$67.04^{+0.21}_{-0.34}$	102.841 ± 0.011
Orbital eccentricity e	0.287 ± 0.062	0.569 ± 0.010
Argument of periastron ω [°]	64 ± 21	63.6 ± 1.4
Orbital inclination i_p [°]	85.55 ± 0.96	$89.1^{+0.6}_{-1.0}$
Transit duration T_{1-4} [hours]	2.699 ± 0.038	1.872 ± 0.025
Primary impact parameter b_prim	0.684 ± 0.032	0.14 ± 0.14
Secondary impact parameter b_sec	1.11 ± 0.23	$0.42^{+0.43}_{-0.30}$
Fitted transit-related parameters:		
System scale $a/R_\star$	$11.8^{+1.4}_{-0.8}$	19.6 ± 0.6
Radius ratio $k = R_\mathrm{p}/R_\star$	0.090 ± 0.002	0.121 ± 0.002
Linear limb darkening coefficient u_a	$0.10^{+0.25}_{-0.17}$	0.53 ± 0.09
Quadratic limb darkening coefficient u_b	0.6 ± 0.4	0.13 ± 0.26
Fitted RV-related parameters:		
Semi-amplitude K [m s^{-1}]	58 ± 7	1288 ± 24
SOPHIE systemic radial velocity $V_\mathrm{0,S}$ [km s^{-1}]	$19.293^{+0.008}_{-0.014}$	-64.235 ± 0.012
HARPS-N systemic radial velocity $V_\mathrm{0,H}$ [km s^{-1}]	19.356 ± 0.008	-64.175 ± 0.050
SOPHIE O-C residuals [m s^{-1}]	35	17
HARPS-N O-C residuals [m s^{-1}]	6	50
Data-related parameters:		
Kepler season 0 contamination [%]	4.5 ± 0.3	10.9 ± 0.4
Kepler season 1 contamination [%]	4.9 ± 0.3	13.7 ± 0.4
Kepler season 2 contamination [%]	5.9 ± 0.3	13.6 ± 0.4
Kepler season 3 contamination [%]	4.7 ± 0.3	10.2 ± 0.4
Kepler season 0 jitter [ppm]	89 ± 12	322 ± 43
Kepler season 1 jitter [ppm]	118 ± 12	329 ± 33
Kepler season 2 jitter [ppm]	101 ± 16	328 ± 36
Kepler season 3 jitter [ppm]	99 ± 14	271 ± 28
SOPHIE jitter [m s^{-1}]	28 ± 13	<8
HARPS-N jitter [m s^{-1}]	<5	<17
Spectroscopic parameters:		
Effective temperature T_eff[K]	6050 ± 110	5330 ± 120
Metallicity [Fe/H] [dex]	0.34 ± 0.14	-0.07 ± 0.15
Stellar rotational velocity $v \sin i_*$ [km s^{-1}]	5.0 ± 1.0	3.5 ± 1.5
Stellar macroturbulence v_macro [km s^{-1}]	2.0 ± 1.0	–
Spectral type	F8V	G8V
Photometric parameter:		
Stellar rotation period [days]	–	19.2 ± 0.3
Stellar physical parameters from combined analysis:		
$M_\star^{1/3}/R_\star$ [solar units]	$0.745^{+0.085}_{-0.051}$	1.084 ± 0.035
Stellar density $\rho_\star$ [g cm^{-3}]	$0.58^{+0.22}_{-0.11}$	1.79 ± 0.17
Star mass $M_\star$ [$M_\odot$]	$1.40^{+0.14}_{-0.11}$	0.88 ± 0.06
Star radius $R_\star$ [$R_\odot$]	1.51 ± 0.14	0.88 ± 0.04
Stellar surface gravity $\log g_*$	4.2 ± 0.1	4.5 ± 0.1
Age of the star [Gyr]	$2.9^{+1.5}_{-0.8}$	6 ± 3
Distance of the system [pc]	1330 ± 170	1140^{+250}_{-160}
Interstellar extinction $E(B-V)$	0.16 ± 0.03	$0.22^{+0.04}_{-0.02}$
Planetary physical parameters from combined analysis:		
Orbital semi-major axis a [AU]	0.084 ± 0.014	0.080 ± 0.005
Periastron distance $(1-e)\,a$ [AU]	0.060 ± 0.011	0.034 ± 0.002
Apoastron distance $(1+e)\,a$ [AU]	0.108 ± 0.019	0.126 ± 0.008
Planet mass M_p [M_Jup]	0.68 ± 0.09	9.9 ± 0.5
Planet radius R_p[R_Jup]	1.32 ± 0.14	1.03 ± 0.06
Planet density ρ_p [g cm^{-3}]	0.37 ± 0.13	11 ± 2
Planetary equilibrium temperature at a-distance $T_{\mathrm{p},a}$ (K)	1250 ± 120	850 ± 40
Planetary equilibrium temperature at periastron $T_\mathrm{p,per}$ (K)	1450 ± 150	1300 ± 60
Planetary equilibrium temperature at apoastron $T_\mathrm{p,apo}$ (K)	1100 ± 110	680 ± 30

we finally derived $e = 0.287 \pm 0.062$. The eccentric solution is ~75 times more probable than the circular. The equilibrium temperatures of the planet derived from $T_{\rm eff}$ and $R_\star$ and assuming an isotropic zero-albedo are $T_{\rm p} = 1450 \pm 150$ K, 1250 ± 120 K, and 1100 ± 110 K at periastron, semi-major axis distance, and apoastron, respectively.

The massive planet KOI-889 b orbits a G8 dwarf star in 8.884924 ± 0.000002 days. Its mass is $9.9 \pm 0.5\ M_{\rm Jup}$ and its radius $1.03 \pm 0.06\ R_{\rm Jup}$. It lies below the deuterium-burning mass (~13 $M_{\rm Jup}$) which could be used to distinguish planets from brown dwarfs. The eccentricity of the orbit is clearly detected in the radial velocities. The value $e = 0.569 \pm 0.010$ could be accurately determined thanks to the large amplitude of the radial velocity variation. The equilibrium temperatures of the planet assuming an isotropic zero-albedo are $T_{\rm p} = 1300 \pm 60$ K, 850 ± 40 K, and 680 ± 30 K at periastron, semi-major axis distance, and apoastron, respectively. Its active host star shows the signature of evolutional spots in the light curve, but the signal-to-noise ratio on the spectra is too low to allow this activity to be detected in the radial velocity jitter or in the core of the Ca II lines. The deduced rotation period is $P_{\rm rot} = 19.2 \pm 0.3$ days which, together with the measured stellar radius, implies a rotation velocity $V_{\rm rot} \simeq 2.3$ km s^{-1}. This is smaller than the value $v \sin i_* = 4.6 \pm 1.0$ km s^{-1} measured from the line widths. This indicates a possible underestimation of the latest value so we adopt $v \sin i_* = 3.5 \pm 1.5$ km s^{-1} as a compromise. If the deduced rotation velocity $V_{\rm rot}$ had been larger than $v \sin i_*$, it would have been consistent with $\sin i_* < 1$, implying an oblique orbit of the planet with respect to the equatorial plane of the star. As this is not the case, there are no signs for spin-orbit misalignment and probably $i_* \simeq i_{\rm p} \simeq 90°$.

For both planets our derived parameters agree with the ones first measured by the *Kepler* team (Borucki et al. 2011a,b; Batalha et al. 2013). An exception is the system scales $a/R_\star$ which we found to be significantly smaller than the ones initially reported from the first *Kepler* light curves because of the unconsidered eccentricities.

4. Tidal evolution

With their orbital periods of 7.34 and 8.88 days, KOI-200 b and KOI-889 b are in a regime where a modest number of transiting planets have been detected. This number has been increasing with the addition of the *Kepler* candidates, but most of these candidates have shallow transits. Only ten transiting giant planets are known today in the period range of 6–50 days. The mass and period of KOI-200 b are similar to those of the three planets WASP-59b, CoRoT-4b, and HAT-P-17b. There are only two nearly analogs of the massive, giant planet KOI-889 b with orbital periods longer than typical periods of hot-Jupiters, namely HAT-P-2b and Kepler-14b (CoRoT-14b is another case of massive, transiting planet, but its orbital period is shorter: 1.5 d). The massive planet KOI-889 b is one of the rare known orbiting a G-type star in a close-in orbit. The lack of planets in that regime was underlined by Bouchy et al. (2011) who proposed that such planets would not survive too close to G dwarfs because of engulfment caused by tidal interactions with the stellar convective zone. If that scenario is correct, KOI-889 b does not follow it.

Both planets KOI-200 b and KOI-889 b are on eccentric orbits and are part of the borderline planets as seen in Fig. 4. Borderline planets are in the period range 6–30 days that lie in the crossover between a regime where the tides are sufficient to explain circularization and a regime where tidal effects are

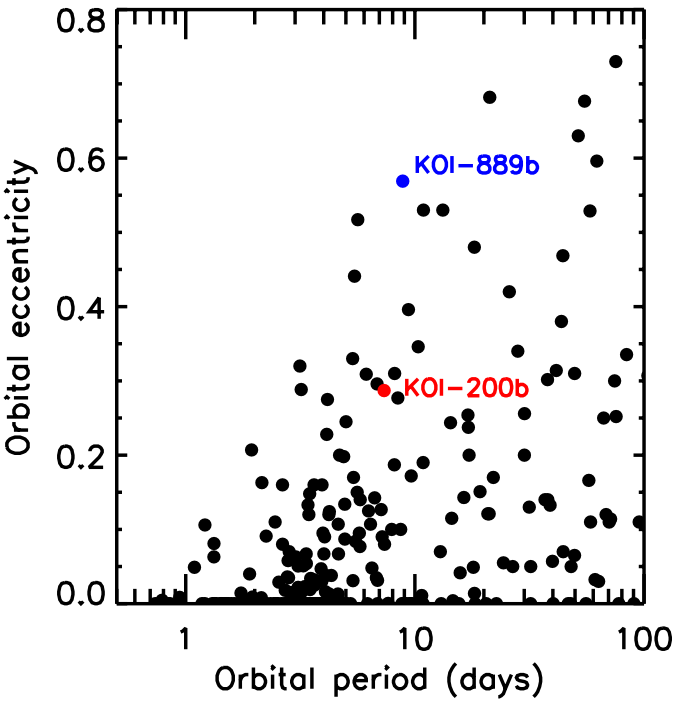

Fig. 4. Orbital eccentricity and period of KOI-200 b and KOI-889 b compared with other known extrasolar planets.

negligible. The dispersion in eccentricity of these systems can be seen as the result of different spin-down rates of young stars, as argued by Dobbs-Dixon et al. (2004). The case of KOI-889 b is particularly interesting since it is close to the envelope of the maximum observed eccentricity for systems in this period range.

Tidal interaction can lead either to a spiralling of the planet into the star followed by a collision, or to the asymptotic evolution towards an equilibrium, characterized by orbital circularity, co-planarity, and co-rotation. Under the assumption that the total angular momentum is conserved (i.e., neglecting magnetic breaking), it can be shown (Hut 1980) that equilibrium states exist only when the total angular momentum of the system $L_{\rm tot}$ is larger than some critical value $L_{\rm crit}$; these equilibrium states are unstable if the orbital angular momentum $h = \sqrt{GM_\star^2 M_{\rm p}^2 a(1-e^2)/(M_\star + M_{\rm p})}$ (where G is the gravitational constant) accounts for less than three quarters of $L_{\rm tot}$. A system that is expected to evolve towards a stable equilibrium is generally called Darwin stable. So far, the vast majority of known exoplanetary systems are not Darwin stable (Matsumura et al. 2010) and their planets will eventually fall into the host star.

In this respect KOI-200 b is not particularly remarkable, despite its eccentricity. Using the stellar rotational velocity $v \sin i_*$ to assess the rotational frequency $\Omega_\star$ of the star (assuming $i_* \simeq 90°$) and taking the gyration radius γ from stellar models for the corresponding mass and temperature (Claret 1995), we can compute the stellar rotational angular momentum, or spin, $L_\star = M_\star(\gamma R_\star)^2 \Omega_\star$. This assumes that the star rotates rigidly and the interior non-uniform distribution of mass is accounted for by γ. For the KOI-200 system, considering the typical value of tidal dissipation efficiency in planets $Q'_{\rm p} = 10^6$ (Matsumura et al. 2008), the timescale for the synchronization and alignment of the planet relative to the orbit is $\sim 4 \times 10^5$ yr, so we can safely assume that the planet is in pseudo-synchronization. Taking the gyration radius of a polytropic model of index 1 for the planet, the planetary spin can also be computed. Adding both

spins to the orbital angular momentum h gives the total angular momentum, which is found to be $L_{\rm tot} \simeq 0.8\,L_{\rm crit}$, so the system is Darwin unstable. The subsequent evolution depends on the relative efficiency of the dissipation of the tides within the star and the planet. Either the dissipation in the planet is dominant and the circularization of the orbit will happen before any significant orbital decay can occur, or it is the efficiency of tidal dissipation in the star that will control the evolution of all the parameters, and the orbit will keep a non-null eccentricity until the engulfment. Finally, little can be inferred from the present state of the system regarding the origin of the eccentricity and the migration scenario. Considering the moderate value of the eccentricity, the lack of constraints on the obliquity, or the presence of a possible companion in the system, either planet-planet scattering or migration in a disk followed by weak tidal interaction is a valid hypothesis. The expected amplitude of the Rossiter-McLaughlin anomaly is $\sim$30 m s^{-1}, so the measurement of the obliquity through the spectroscopic observation of a transit is feasible.

On the other hand, KOI-889 b is much more interesting. The rotation period of its host star is estimated to be $P_{\rm rot} = 19.2 \pm 0.3$ days (Sect. 2.1). Using the same reasoning as described above, we find that the system has $L_{\rm tot} \simeq 1.3\,L_{\rm crit}$, thus allowing for the existence of equilibrium states. Furthermore, $h/L_{\rm tot} \simeq 0.9904$, meaning that the system is evolving toward a stable equilibrium. Considering that $n/\Omega_\star \simeq 2$ (where n is the mean orbital motion), we know that tides act to bring the planet closer to the star while circularizing the orbit. Moreover, in the frame of the weak friction model of the equilibrium tides with constant time lag, the main global features of tidal evolution can be derived, using energy and angular momentum considerations only (Hut 1981). It turns out that the only external parameter of the coupled differential equations that rule the temporal behavior of the orbital parameters is α, the ratio of the orbital and rotational angular momentum of the system at the stable equilibrium. For KOI-889 b, $\alpha \simeq 22.8$, allowing for the existence of turning points in the evolution of both the semi-major axis and the eccentricity. The past and future evolution of the system can thus be non-monotonic (see Fig. 5). Considering that KOI-889 is a G8V star showing clear evidence of magnetic activity, this problem is further complicated by the effect of stellar magnetic braking, which is not taken into account in the derivation by Hut (1981), but which makes the star spin down (Dobbs-Dixon et al. 2004).

The fact that $n/\Omega_\star \simeq 2$ is intriguing because it is the value where Type II migration stops if the disk is truncated at the corotation radius (Kuchner & Lecar 2002). Assuming that this migration mechanism is indeed the dominant one for KOI-889 b, this would be evidence that the tidal interactions in this system from the time of the disappearance of the disk are either weak or that the system is young. The rotation period of the star invalidates the former interpretation because young stars are observed to rotate significantly faster, meaning that some tidal interaction must have occurred to preserve the synchronization. Moreover, in both cases the significant eccentricity of the orbit is difficult to explain because Type II migration tends to produce circular systems (e.g., Benítez-Llambay et al. 2011). However, if we consider that the star was still in its pre-main-sequence phase when the disk disappeared (Mamajek 2009), the rapid increase of the spin of the star caused by the contraction of the radius can lead the system into a domain where the eccentricity can be excited while the orbit would widen, assuring the survival of the planet. The subsequent evolution would see the spin loss of the star caused by magnetic braking bring the system progressively in the domain where both the eccentricity and the semi-major axis are damped toward a stable equilibrium. However, the angular momentum extracted from the system by magnetic braking will eventually make the system Darwin unstable. Depending on the relative efficiency of tidal dissipation and magnetic braking, this might cause the planet to spiral into its host before the end of the main sequence lifetime of the star.

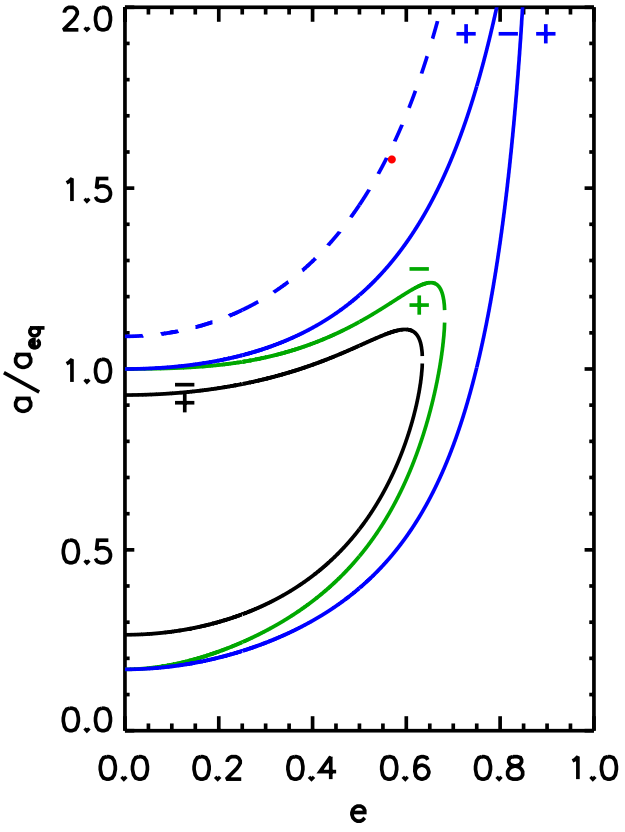

Fig. 5. Regions of different types of tidal evolution for the planetary system KOI-889, neglecting magnetic braking following Hut (1981). The semi-major axis a is normalized to its value at the stable equilibrium $a_{\rm eq}$. The black, solid line gives the stationary points of the eccentricity, with the plus and minus signs indicating the domains where the eccentricity increases and decreases, respectively. The green and blue solid lines give the corresponding information for the semi-major axis and rotational angular velocity of the star, respectively. The dashed, blue line separates the upper region where $\Omega_\star < 0$ from the lower region where $\Omega_\star > 0$. The red dot is the present state of the system, corresponding to an evolution where $\mathrm{d}\Omega_\star/\mathrm{d}t > 0$, $\mathrm{d}a/\mathrm{d}t < 0$, and $\mathrm{d}e/\mathrm{d}t < 0$.

Although the age of the star KOI-889 is not well constrained, a detailed study could give useful constraint on the efficiency of the tidal dissipation in both the star and planet, as well as an estimate of the loss of angular momentum through magnetic braking. For the massive planet KOI-889 b, a direct obliquity measurement would be useful to confirm the correlation between spin-orbit misalignment and planetary mass suggested by Hébrard et al. (2011a,b). Indeed, KOI-889 b is one of the few known transiting planets in that range of radius and mass, together with HAT-P-2b, CoRoT-14b, and Kepler-14b. Comparison between $v \sin i_*$ and $P_{\rm rot}$ does not suggest any spin-orbit misalignment in the KOI-889 system, whose expected amplitude of the Rossiter-McLaughlin anomaly is $\sim$40 m s^{-1}.

5. Conclusion

We have presented the detection and characterization of KOI-200 b and KOI-889 b, two new transiting, close-in, giant

extrasolar planets. They were first detected as promising candidates by the *Kepler* team from *Kepler* light curves. We have established their planetary nature with the radial velocity follow-up we jointly secured using both the spectrographs SOPHIE and HARPS-N, and characterized them through combined analyses of the whole photometric and spectroscopic datasets. The planet KOI-200 b orbits its F8V host star in 7.34 days and its mass and radius are $0.68 \pm 0.09\ M_{\rm Jup}$ and $1.32 \pm 0.14\ R_{\rm Jup}$. KOI-889 b is a massive planet orbiting in 8.88 days an active G8V star with a rotation period of 19.2 ± 0.3 days; its mass and radius are $9.9 \pm 0.5\ M_{\rm Jup}$ and $1.03 \pm 0.06\ R_{\rm Jup}$. Both planets lie on eccentric orbits and are located just at the frontier between regimes where the tides can explain circularization and where tidal effects are negligible, making them interesting systems with respect to tidal evolution. The planet KOI-200 is another example that is already Darwin unstable, whereas KOI-889 is one of the few known Darwin-stable exoplanetary systems. After the announcement of the present results, the *Kepler* Team gave to KOI-200 and KOI-889 the names Kepler-74 and Kepler-75, respectively.

Since its installation in Spring 2012 at the Telescopio Nazionale *Galileo*, HARPS-N has allowed the obliquity of the transiting planet Qatar-1 b to be measured (Covino et al. 2013) and has shown that the metal-poor star HIP 11952 does not harbor giant planets (Desidera et al. 2013). The two new planets KOI-200 b and KOI-889 b presented here are the first to be detected and characterized with HARPS-N. Our observing program managed jointly with SOPHIE and HARPS-N shows the benefits that could be obtained for the follow-up of transiting planet candidates from coordinated observations secured with two spectrographs with different sensitivities, precisions, and accessibilities.

Acknowledgements. This publication is based on observations collected with the NASA satellite *Kepler*, the SOPHIE spectrograph on the 1.93-m telescope at *Observatoire de Haute-Provence* (CNRS), France (program 12A.PNP.MOUT), and the HARPS-N spectrograph on the 3.58-m Italian Telescopio Nazionale *Galileo* (TNG) operated on the island of La Palma by the Fundación Galileo Galilei of the INAF (Istituto Nazionale di Astrofisica) at the Spanish Observatorio del Roque de los Muchachos of the Instituto de Astrofisica de Canarias (program OPT12B_13 from OPTICON common time allocation process for EC supported trans-national access to European telescopes). The authors particularly thank the *Kepler*, OHP, and TNG teams, whose work and expertise allowed these results to be obtained. This publication also makes use of data products from 2MASS, which is a joint project of the University of Massachusetts and the Infrared Processing and Analysis Center/California Institute of Technology, funded by NASA and the NSF, as well as data products from WISE, which is a joint project of the University of California and the JPL/MIT, funded by NASA. Funding for SDSS-III has been provided by the Alfred P. Sloan Foundation, the Participating Institutions, the NSF, and the U.S. Department of Energy Office of Science. The research leading to these results has received funding from the "Programme National de Planétologie" (PNP) of CNRS/INSU, and from the European Community's Seventh Framework Programme (FP7/2007-2013) under grant agreement number RG226604 (OPTICON). AS acknowledges the support by the European Research Council/European Community under the FP7 through Starting Grant agreement number 239953 and the support from Fundação para a Ciência e a Tecnologia (FCT) in the form of grant reference PTDC/CTE-AST/098528/2008. RFD is supported by CNES.

References

Almenara, J. M., Deeg, H. J., Aigrain, S., et al. 2009, A&A, 506, 337
Allard, F., Homeier, D., & Freytag, B. 2012, IAU Symp., 282, 235
Baranne, A., Queloz, D., Mayor, M., et al. 1996, A&AS, 119, 373
Barnes, S. A. 2007, ApJ, 669, 1167
Batalha, N. M., Rowe, J. F., Bryson, S. T., et al. 2013, ApJS, 204, 24
Benítez-Llambay, P., Masset, F., & Beaugé, C. 2011, A&A, 528, A2
Boisse, I., Eggenberger, A., Santos, N. C., et al. 2010, A&A, 523, A88
Bonomo, A. S., Hébrard, G., Santerne, A., et al. 2012, A&A, 538, A96
Borucki, W. J., Koch, D. G., Basri, G., et al. 2011a, ApJ, 728, 117
Borucki, W. J., Koch, D. G., Basri, G., et al. 2011b, ApJ, 736, 19
Bouchy, F., Moutou, C., Queloz, D., et al. 2009a, IAU Symp., 253, 129
Bouchy, F., Hébrard, G., Udry, S., et al. 2009b, A&A, 505, 853
Bouchy, F., Bonomo, A. S., Santerne, A., et al. 2011, A&A, 533, A83
Bouchy, F., Díaz, R. F., Hébrard, G., et al. 2013, A&A, 549, A49
Brown, T. M., Latham, D. W., Everett, M. E., & Esquerdo, G. A. 2011, AJ, 142, 112
Bruntt, H., Bedding, T. R., Quirion, P.-O., et al. 2010, MNRAS, 405, 1907
Burke, C. J., Bryson, S., Christiansen, J., et al. 2013, AAS #221, 216.02
Claret, A. 1995, A&AS, 109, 441
Claret, A., Hauschildt, P. H., & Witte, S. 2012, A&A, 546, A14
Colòn, K. D., Ford, E. B., & Morehead, R. C. 2012, MNRAS, 426, 342
Cosentino, R., Lovis, C., Pepe, F., et al. 2012, SPIE Proc., 8446E
Covino, E., Esposito, M., Barbieri, M., et al. 2013, A&A, 554, A28
Csizmadia, Sz., Pasternacki, Th., Dreyer, C., et al. 2013, A&A, 549, A9
Desidera, S., Sozzetti, A., Bonomo, A., et al. 2013, A&A, 554, A29
Díaz, R. F., Damiani, D., Deleuil, M., et al. 2013, A&A, 551, L9
Dobbs-Dixon, I., Lin, D. N., & Mardling, R. A. 2004, ApJ, 610, 464
Ehrenreich, D., Lagrange, A.-M., Bouchy, F., et al. 2011, A&A, 525, A85
Espinosa Lara, F., & Rieutord, M. 2012, A&A, 547, A32
Etzel, P. B. 1981, in Photometric and Spectroscopic Binary Systems, Proc. NATO Advanced Study Institute, 111
Ford, E. B. 2006, ApJ, 642, 505
Fressin, F., Torres, G., Charbonneau, D., et al. 2013, ApJ, 766, 81
Gilliland, R. L., Chaplin, W. J., Dunham, E. W., et al. 2011, ApJS, 197, 6
Hébrard, G., Ehrenreich, D., Bouchy, F., et al. 2011a, A&A, 527, L11
Hébrard, G., Désert, J.-M, Díaz, R. F., et al. 2011b, A&A, 516, A95
Hébrard, G., Collier Cameron, A., Brown, D. J. A., et al. 2013, A&A, 549, A134
Hut, P. 1980, A&A, 92, 167
Hut, P. 1981, A&A, 99, 126
Jenkins, J. M., Caldwell, D. A., Chandrasekaran, H., et al. 2010, ApJ, 713, L87
Kipping, D. M. 2010, MNRAS, 408, 1758
Kipping, D., & Bakos, G. 2011, ApJ, 730, 50
Kostov, V. B., McCullough, P., Hinse, T., et al. 2013, ApJ, 770, 52
Kuchner, M. J., & Lecar, M. 2002, ApJ, 574, L87
Lagarde, N., Decressin, T., Charbonnel, C., et al. 2012, A&A, 543, A108
Lanza, A. F. 2010, A&A, 512, A77
Mamajek, E. E. 2009, AIP Conf. Ser., 1158, 3
Matsumura, S., Takeda, G., & Rasio, F. 2008, ApJ, 686, L29
Matsumura, S., Peale, S. J., & Rasio, F. A. 2010, ApJ, 725, 1995
Morton, T. D., & Johnson, A. A. 2011, ApJ, 738, 170
Pepe, F., Mayor, M., Galland, F., et al. 2002, A&A, 388, 632
Perruchot, S., Kohler, D., Bouchy, F., et al. 2008, SPIE Proc., 70140J
Santerne, A., Díaz, R. F., Bouchy, F., et al. 2011a, A&A, 528, A63
Santerne, A., Bonomo, A. S., Hébrard, G., et al. 2011b, A&A, 536, A70
Santerne, A., Díaz, R. F., Moutou, C., et al. 2012, A&A, 545, A76
Santerne, A., Fressin, F., Díaz, R. F., et al. 2013, A&A, submitted
Southworth, J., Maxted, P. F. L., & Smalley, B. 2004, MNRAS, 351, 1277
Tegmark, M., Strauss, M. A., Blanton, M. R., et al. 2004, Phys. Rev. D, 69, 103501
Valenti, J. A., & Fisher, D. A. 2005, ApJS, 159, 141
Valenti, J. A., & Piskunov, N. 1996, A&AS, 118, 595
Winn, J. N. 2010 [arXiv:1001.2010]